ADVANCING EARTH AND SPACE SCIENCE

JGR Solid Earth

RESEARCH ARTICLE

10.1029/2021JB022650

Key Points:

- We observe both coseismic *dv/v* drops and strong seasonal *dv/v* variations through a 20-year systematic analysis in Taiwan
- The rainfall-induced pore pressure change is likely the primary control of the seasonal *dv/v* variations in the crust
- Evaluating the environmental influences on *dv/v* allows us to isolate crustal damage related to earthquakes

Supporting Information:

Supporting Information may be found in the online version of this article.

Correspondence to:

H.-H. Huang and K.-F. Feng,
hhhuang@earth.sinica.edu.tw;
kuanfufeng@earth.sinica.edu.tw

Citation:

Feng, K.-F., Huang, H.-H., Hsu, Y.-J., & Wu, Y.-M. (2021). Controls on seasonal variations of crustal seismic velocity in Taiwan using single-station cross-component analysis of ambient noise interferometry. *Journal of Geophysical Research: Solid Earth*, *126*, e2021JB022650. https://doi.org/10.1029/2021JB022650

Received 21 JUN 2021
Accepted 19 OCT 2021

Author Contributions:

Conceptualization: Hsin-Hua Huang
Data curation: Kuan-Fu Feng, Ya-Ju Hsu
Formal analysis: Kuan-Fu Feng
Funding acquisition: Hsin-Hua Huang
Investigation: Kuan-Fu Feng, Hsin-Hua Huang
Methodology: Kuan-Fu Feng, Hsin-Hua Huang
Software: Kuan-Fu Feng, Hsin-Hua Huang
Supervision: Hsin-Hua Huang, Yih-Min Wu
Validation: Kuan-Fu Feng, Ya-Ju Hsu
Writing – original draft: Kuan-Fu Feng

Controls on Seasonal Variations of Crustal Seismic Velocity in Taiwan Using Single-Station Cross-Component Analysis of Ambient Noise Interferometry

Kuan-Fu Feng[1], Hsin-Hua Huang[2], Ya-Ju Hsu[2,1], and Yih-Min Wu[1,2,3]

[1]Department of Geosciences, National Taiwan University, Taipei, Taiwan, [2]Institute of Earth Sciences, Academia Sinica, Taipei, Taiwan, [3]Research Center for Future Earth, National Taiwan University, Taipei, Taiwan

Abstract Ambient noise interferometry is a powerful technique to continuously measuring crustal seismic velocity changes (*dv/v*) and studying crustal behaviors over time. However, the interpretation of such *dv/v* variations is not straightforward since multiple causes including internal (tectonic/magmatic) processes of the crust and external (environmental) factors could both affect *dv/v* simultaneously. To differentiate the interplay between the internal and external processes in *dv/v* variations is an essential step toward accurate crustal monitoring. In this study, we apply the single-station cross-component (SC) method to 15 selected stations from the Broadband Array in Taiwan for Seismology (BATS) to investigate the temporal evolution of crustal seismic velocities across Taiwan. We process the continuous BATS seismic recording from 1998 to 2019, construct the daily SC correlation functions, and compute *dv/v* values by the stretching technique in a frequency band of 0.1–0.9 Hz. We observe both strong annual *dv/v* variations and co-seismic velocity drops associated with regional moderate-to-large earthquakes. Systematic spectral and time-series analyses with the weather data suggest that the rainfall-induced pore-pressure change plays a predominant role in driving the *dv/v* seasonality, reflecting a diffusion process from meteoric water into shallow crust. The effects of other factors are relatively local and secondary. We also demonstrate how understanding and correcting rainfall effects could critically improve the resolution and accuracy of internal crustal damage related to earthquakes.

Plain Language Summary The measured wave speeds from small ground motions such as ocean, wind, traffic, etc help us to understand changes in subterranean regions. The causes of the medium changes are multifold such as the fault zone damage by earthquakes (internal) or groundwater rise by rainfall (external). To discriminate the causes it is important to use weak ground motions for monitoring internal medium changes. For this purpose, we collect and study 20 years of ground motion data from 15 seismic stations distributed across Taiwan. We measure the propagation wave speed of weak ground motions and find earthquake-related changes and strong seasonal changes at most stations. By analyzing and comparing wave speed changes with weather data (e.g., rainfall, temperature, air pressure, and wind speed), we find that rainfall varying groundwater level and the subterranean pore pressure best fit the seasonal wave speed changes in both space and time. After removing this rainfall-related signals, we can estimate more precisely the extent of earthquake-related underground damages that may not be obvious or completely masked by the strong seasonal changes.

1. Introduction

Ambient noise interferometry has been widely used to detect seismic velocity changes (*dv/v*) in response to internal crustal processes, such as volcanic unrests (Brenguier, Shapiro, et al., 2008; Feng et al., 2020; Obermann, Planès, Larose, & Campillo, 2013; Olivier et al., 2019), fault zone damage and healing (Brenguier, Campillo, et al., 2008; Hillers et al., 2019; Liu et al., 2018; Obermann et al., 2014; Viens et al., 2018; Wang et al., 2019; Wegler & Sens-Schönfelder, 2007; Yu & Hung, 2012), basin water storage (Berbellini et al., 2021; Clements & Denolle, 2018; Lecocq et al., 2017), and ice sheet loading/melting dynamics (Mordret et al., 2016). Such seismic velocity variations are also known to be complex since they could originate from multiple concurrent causes including external environmental forces. For instance, *dv/v* has been found to correlate with precipitation, groundwater level, atmospheric pressure, temperature, snow depth, and tidal height (Andajani et al., 2020; Clements & Denolle, 2018; Donaldson et al., 2019; Hillers

Writing – review & editing: Hsin-Hua Huang, Ya-Ju Hsu, Yih-Min Wu

et al., 2014, 2015; Mao et al., 2019; Richter et al., 2014; Sens-Schönfelder & Wegler, 2006; Wang et al., 2017). Environmental-induced periodic *dv/v* signals observed in northern Chile (Richter et al., 2014), Germany (Lecocq et al., 2017), Japan (Wang et al., 2017), Iceland (Donaldson et al., 2019), the central United States (Liu et al., 2020), and other regions have shown different controlling factors varying from place to place and complicated the interpretations of *dv/v* for internal changes of the crust. Thus, understanding and differentiating the interplay of internal (e.g., magmatic, tectonic) and external (e.g., environmental) processes in *dv/v* variations is an important step toward not only more accurate crustal monitoring but also finding hidden signals. For a more comprehensive discussion, we refer readers to a recent review of Le Breton et al. (2021).

As an active orogenic belt in the subtropical zone, Taiwan is one of few places in the world that features strong interactions of environmental and tectonic processes with high seismicity rate and distinct dry and wet seasons (Hsu et al., 2021; Steer et al., 2020). Yu and Hung (2012) investigated the coseismic velocity changes associated with the 2006 Taitung earthquake in southeastern Taiwan and found negative correlations between rainfall, groundwater level variations, and *dv/v*, in addition to the coseismic velocity drop. Using the borehole array of the Taiwan Chelungpu-fault Drilling Project (TCDP) data, Hillers et al. (2014) found that the hydraulic properties play a governing role of *dv/v* variations. However, an island-wide and systematic analysis is still lacking. However, an island-wide and systematic analysis is still lacking. More than two decades of data recorded by the Broadband Array in Taiwan for Seismology (BATS; Institute of Earth Sciences, Academia Sinica, 1996) provide a great opportunity to investigate the long-term dv/v variations in the crust across Taiwan (Figure 1a).

In this study, we apply a single-station cross-components (SC) analysis to continuous BATS seismic recordings from 1998 to 2019. We observe a clear co-seismic velocity drop associated with the 1999 M_w 7.6 Chi-Chi earthquake and strong periodic variations of *dv/v* at most stations (Figures 1b–1e). To investigate the causes of *dv/v* periodicity, we conduct comparative analyses in the frequency and time domains between the *dv/v* variations and the environmental data from nearby weather stations including rainfall, temperature, air pressure, and wind speed (Figure 1a). We also model the rainfall-induced pore pressure changes and groundwater level to investigate the hydrological process in the shallow crust. The results suggest a predominant role of rainfall in causing *dv/v* variations across Taiwan. The modeled pore pressure changes well predict the main trends of the *dv/v* (with high correlation coefficients around 0.6–0.8) for most stations in the foothill and mountainous areas and reflect a diffusion process from meteoric water into shallow crust. By correcting rainfall effects from *dv/v*, we improve the detection capability of the internal tectonic processes associated with earthquakes.

2. Materials and Methods

2.1. Seismic Data and Ambient Noise Interferometry

We analyze the three-component continuous data in 1998–2019 from 15 broadband seismic stations of the BATS network, which are selected to be uniformly distributed across Taiwan (Figure 1a, blue triangles). The data completeness is shown in Figure S1. We closely follow the processing procedure described in Feng et al. (2020) which cuts the continuous data into daily subsets, removes instrumental response, demeans, detrends, tapers, and decimates the data to 20 Hz. The spectral whitening (Bensen et al., 2007) and Welch's method (Seats et al., 2012) which uses 5-min moving time windows with 50% overlaps are applied to compute 150-s time lag correlation functions. The main difference of our work from Feng et al. (2020) is that we focus on single station cross-component correlations (that include ZN, ZE,NZ, NE, EZ, and EN) rather than station pair cross correlations (CC) because it is more straightforward and accurate for comparing it to data from nearby weather stations. The SC has also been demonstrated to be more stable than the autocorrelation (AC) method (De Plaen et al., 2016; Donaldson et al., 2019; Hobiger et al., 2014).

After computing daily SC functions (SCFs), we then applied a 30-day backward stacking for each day to gain better signal-to-noise ratios (SNR) and coherence between SCFs (Figure 2). A reference SCF is constructed by stacking all available SCFs over the entire study period. The time shifts (dt/t) in windowed coda waves between daily SCFs and the reference SCF are then measured to infer the average seismic velocity changes (dv/v) of the medium around that station via the equation (Snieder et al., 2002):

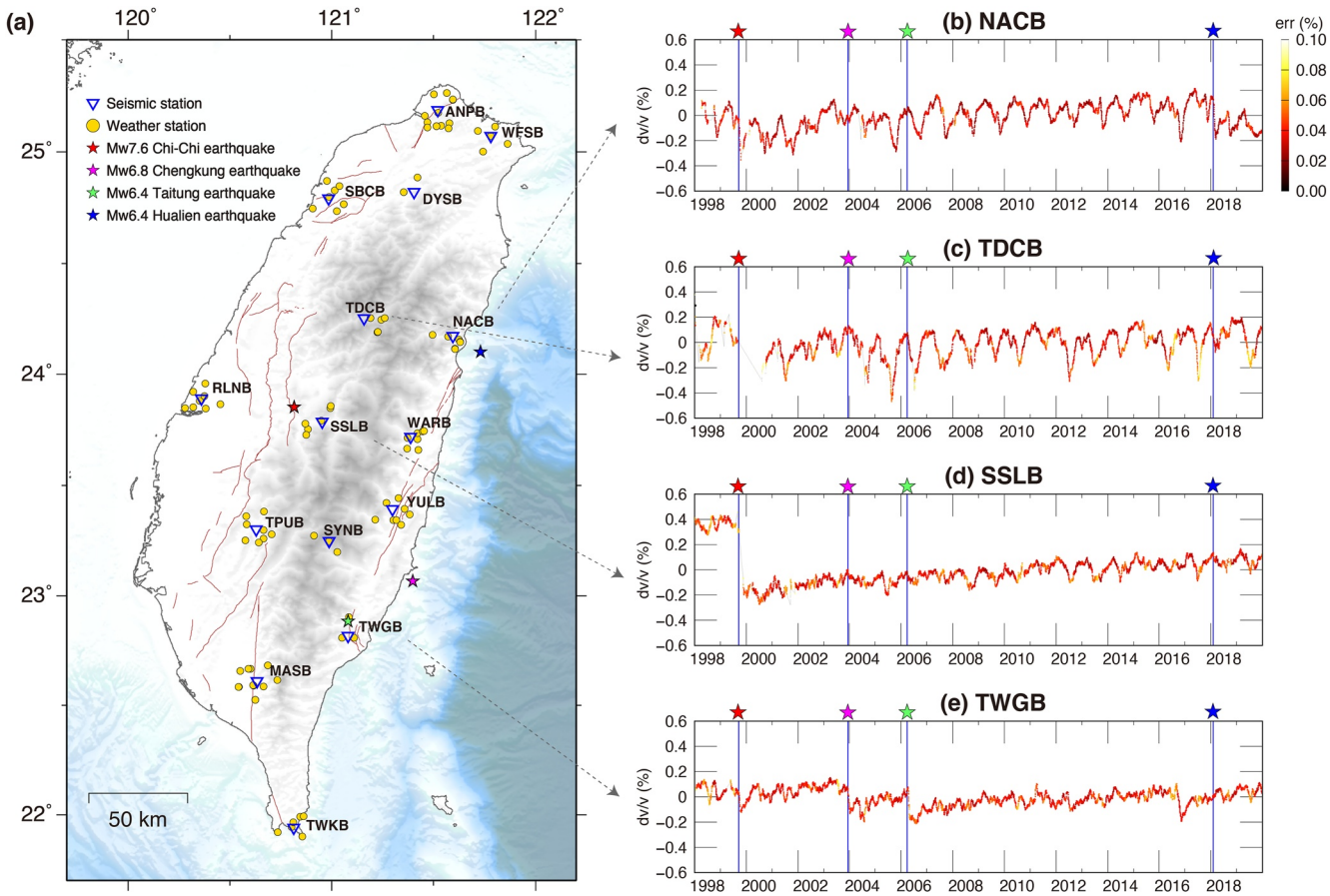

Figure 1. Station distribution and time series of seismic velocity changes (dv/v). (a) Distribution of seismic stations (reversed triangles) and selected weather stations for Gaussian smoothing analysis (yellow dots). Red lines mark the active faults defined by the Central Geology Survey, Taiwan. The stars represent the hypocenter location of the 1999 Chi-Chi (M_w 7.6), 2003 Chengkung (M_w 6.8), 2006 Taitung (M_w 6.4), and 2018 Hualien (M_w 6.4) earthquakes. (b–e) The temporal evolutions of dv/v at Station NACB, TDCB, SSLB, and TWGB selected for illustration. The blue lines mark the occurrence time of earthquakes as indicated by starts in (a).

$$dt/t = -dv/v. \tag{1}$$

To determine the optimal length of the coda time window, we filter the SCFs to 0.1–0.9 Hz and compute the moving window cross-correlation over the entire 150-s time lag between daily SCFs and the reference SCF using a 20-s window with 1-s moving step. The results show that the correlation coefficient values become lower than 0.8 when the lag time is greater than 60 s for most stations (Figure S2). Therefore, we use a 50-s coda window that begins at 10 s of the lag time to avoid the first wavelength of the large source wavelet centered at zero time (Figure 2).

We use both the stretching method (Sens-Schönfelder & Wegler, 2006) and the moving-window cross-spectrum method (MWCS, Clarke et al., 2011) to calculate and cross-validate the dv/v measurements. While the stretching method was known to be affected by the change of frequency content in ambient noise (Zhan et al., 2013), estimates of dv/v are similar to but more stable than those measured by the MWCS in general (Figure S3). We therefore use the stretching dv/v measurements for later analysis.

Based on a theoretical formulation of the apparent stretching factor (Weaver et al., 2011), we also calculate the uncertainty of the estimated dv/v for each component combination. The uncertainties are then used to compute a weighted average of dv/v at all six component combinations to form the final dv/v results. When averaging, only the dv/v results with a cross-correlation value greater than 0.6 (from stretching method) are used.

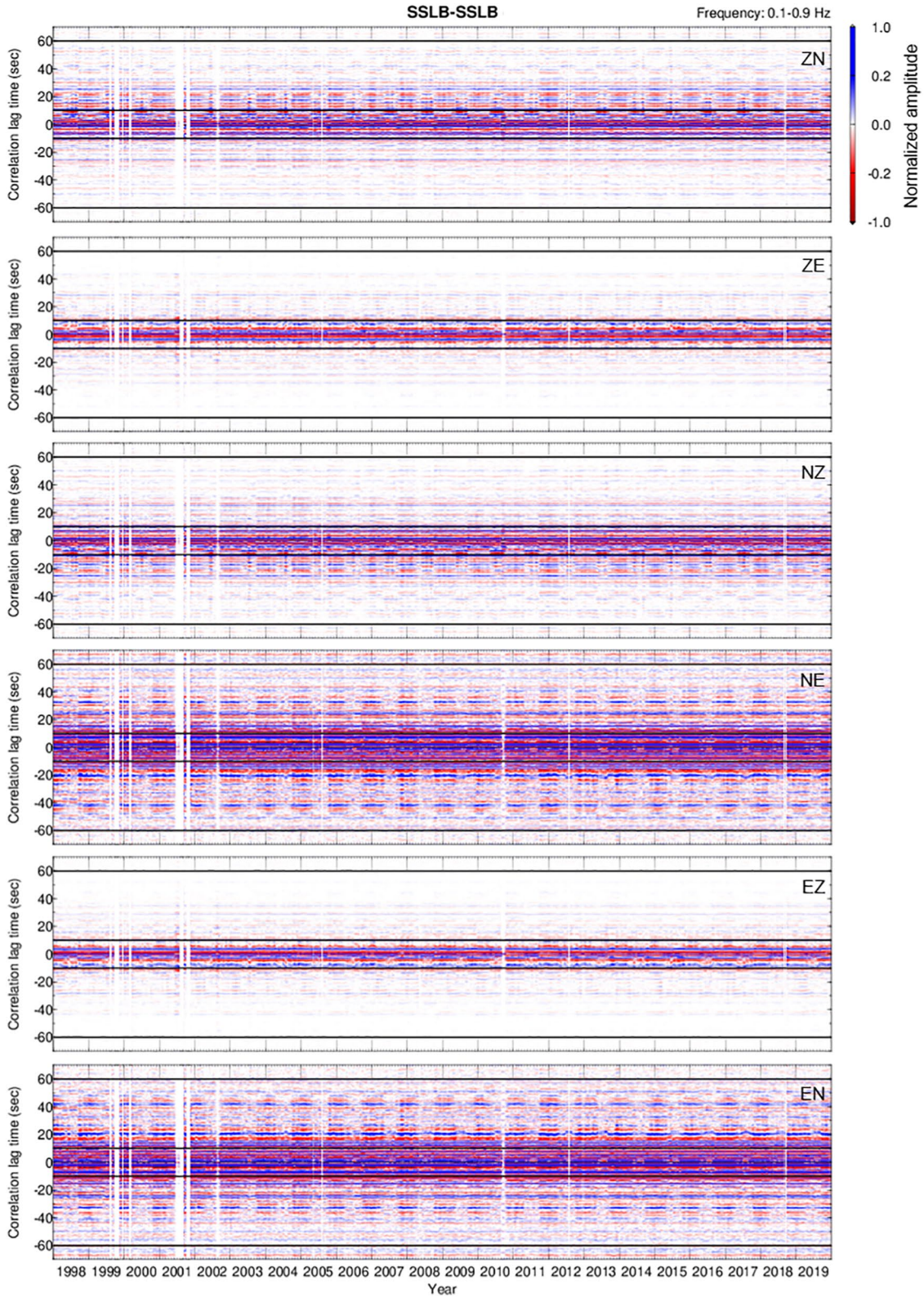

Figure 2. An example of cross-component correlations of single station (SC) at Station SSLB. The black boxes denote the coda windows used for *dv/v* measuring. Different cross-component correlation functions are normalized by the peak amplitude of their reference correlation functions (RCF), respectively.

2.2. Depth Sensitivity Kernels

In a multiple scattering regime, the wave propagation acts like a random walk process and can be described by a diffusion equation (Pacheco & Snieder, 2005; Planès et al., 2014). On the assumption that the early coda waves are dominated by surface waves (Obermann, Planes, Larose, Sens-Schönfelder, et al., 2013; Obermann et al., 2016), we assume that the coda is mainly composed of Rayleigh wave energy and calculate the depth sensitivity kernels of frequency bands between 0.1 and 0.9 Hz (Herrmann, 1987). This Rayleigh wave sensitivity to the depth of the velocity perturbation, while has often been assumed, was also validated recently in a numerical work of Yuan et al. (2021). Given a 1-D velocity model averaged from a recent local 3-D velocity model (Huang et al., 2014), the calculated Rayleigh wave sensitivity kernels for different frequencies are shown in Figure S4. The frequency band of 0.1–0.9 Hz used in this study is mostly sensitive to the medium changes from the surface to the depth of about 3 km.

2.3. Weather Data and Data Processing

Figure S5a shows the distribution of the weather stations operated by the Central Weather Bureau (CWB) in Taiwan. The weather stations provide the hourly data of rainfall, air pressure, air temperature, and wind speed. We convert these hourly weather data to daily data. For rainfall, we calculate the cumulative rainfall each day. For the other three, we calculate the daily average.

Since the multiply scattering coda waves sample a finite volume of the medium, we calculate their lateral sensitivity to be 10.7 km based on the first Fresnel zone assumption (Bennington et al., 2018). The weather stations within a radius of 10.7 km of each seismic station are selected. We then apply spatial Gaussian smoothing (with a standard deviation of 10.7 km) to the selected stations to obtain averaged weather data to compare with the dv/v measurements. Figure 1 shows the locations of the selected weather stations (yellow circles) for each seismic station (blue triangles). Note that not all the weather stations have all four types of data throughout the entire study period, and rainfall data is usually the most complete one among them all (Figure 3).

3. Results and Analysis

3.1. Seasonal Variations of dv/v and Weather Data

The strong periodic dv/v variations are perceived at most stations over the entire period from 1998 to 2019 (Figures 1b–1e). The peak-to-peak amplitude of periodic dv/v variations ranges from 0.02% to 0.2% (Figure S6), which is roughly consistent with the dv/v range of 0.01%–0.1% for the frequency band of 0.1–1 Hz in Le Breton et al. (2021). The time series of dv/v and weather data consistently have periodic cycles like in the example shown by Station MASB (Figure 3). We convert the time series data into normalized spectra to investigate their dominant periods (Figure 4). In the spectrum, the strongest signal appears at a cycle of one year in the observed dv/v and all weather data. Relatively broader bandwidth of temperature, air pressure, and wind speed in the spectrum is due to shorter periods of data available (Figures 3c–3e). The rain-related Madden-Julian Oscillation (MJO) signals around 60–80 days, as found at TCDP borehole array (Hillers et al., 2014), appear in the rainfall records at some stations (e.g., Station NACB, TDCB, WFSB) but do not reflect on our dv/v time series. The 30-day-long stacking may likely mute possible MJO-related dv/v signals to some degree. However, the exact reason the MJO footprint is not reflecting on dv/v is beyond the scope of this study. While a semiannual cycle could also be observed in dv/v and rainfall, we focus our discussion mainly on annual signals (Figure 3).

Since all the weather factors exhibit annual cycles, we perform an annual stack for all the data to compare their behavior for an average year (Figure 5). A 30-day low-pass filtering is applied to remove short-wavelength disturbances (light-color thin curves) and only retain the primary long-wavelength features (dark-color thick curves) before stacking. In Figure 5, we select four representative stations MASB, NACB, TDCB, and WFSB for the southern, eastern, central, and northern regions of Taiwan, respectively. Each subplot of Figure 5 includes the annual stacks of normalized dv/v (black), rainfall (blue), temperature (orange), air pressure (purple), and wind speed (green). Notably, the annual dv/v variations show strong site-dependent features. At the station MASB, the dv/v first increases from January to May, then drops to the lowest level in

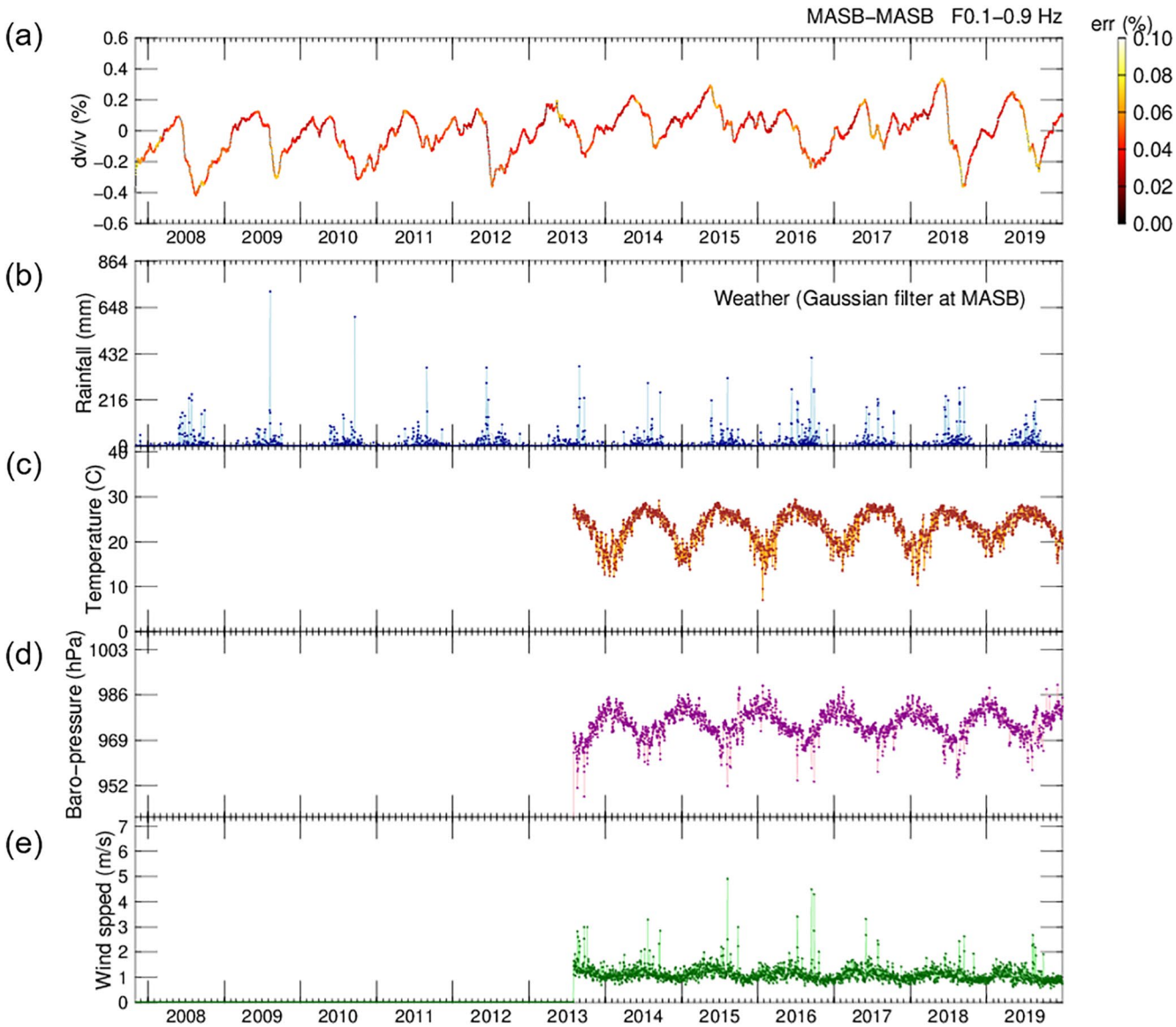

Figure 3. An example of *dv/v* time series at Station MASB and weather data averaged from the adjacent sites. (a) The *dv/v* with color-coded errors, (b) rainfall, (c) temperature, (d) air pressure, and (e) wind speed.

September, and finally increases from October to December. At the station NACB, the trend of *dv/v* is similar to the station MASB, but the lowest value of *dv/v* occurs in late October. At the station TDCB, the *dv/v* first shows a decreasing trend from late January to July, then drops to a minimum in July, and finally increases toward winter. At the station WFSB, the temporal pattern of *dv/v* is almost opposite to that in TDCB, the *dv/v* gradually increases in January to May at first, then attains its highest value in May to August, and finally decreases toward winter.

In contrast, the annual variations of temperature and air pressure are similar across four stations, although with different amplitudes. Annual stacked temperature shows an increasing trend in the first half year, followed by a decreasing trend in the second half year with a peak-to-peak amplitude of 14°C. Air pressure exhibits an opposite temporal pattern to temperature and the annual peak-to-peak amplitude is less than 16 hPa. Because the wind speed changes could also interact with local topography and modulate the noise wavefield locally to cause spurious *dv/v* signals (Hillers & Ben-Zion, 2011; Hillers et al., 2015), we also compare the wind speed with *dv/v*. There is considerable diversity in the temporal patterns of annually stacked

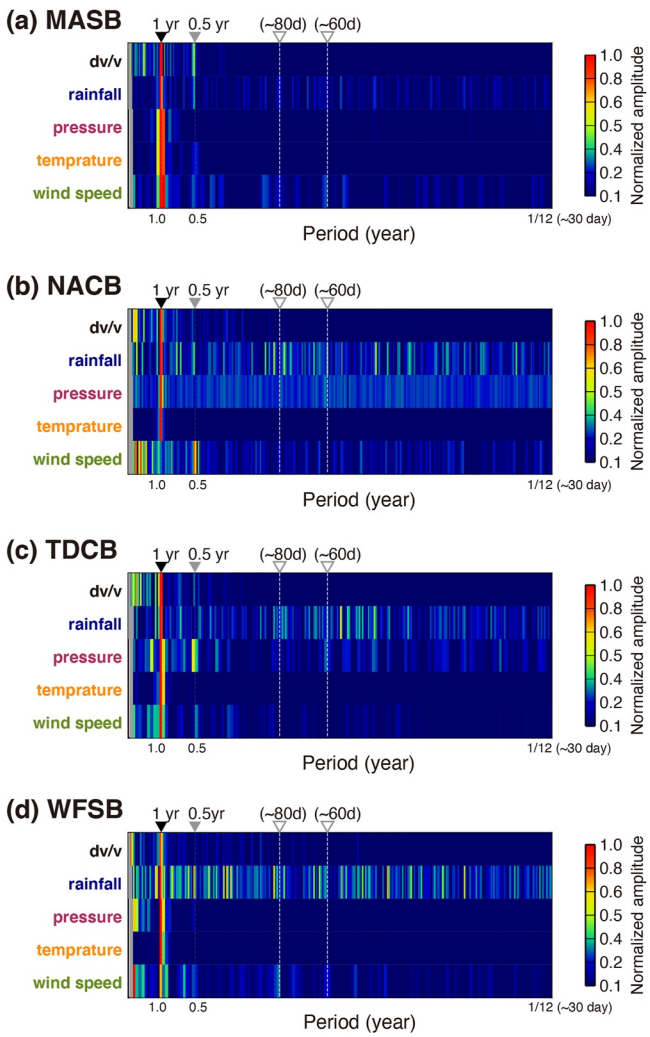

Figure 4. Examples of the normalized spectrum at the stations (a) MASB, (b) NACB, (c) TDCB, and (d) WFSB. From top to bottom are the observed *dv/v*, rainfall, air temperature changes, air pressure changes, and wind speed changes. Black and gray triangles mark the period of one and half year. The Madden–Julian Oscillation (MJO) of 60–80 days cycles is marked by an open triangle (Hillers et al., 2014).

wind speed data with the amplitudes ranging from 0.1 to 0.5 m/s, but no consistent correlation with *dv/v* is found. The rainfall also shows different annual patterns across stations. A clear dry-rainy season is shown at two stations MASB and NACB, with the dry season in winter and spring and the rainy season in summer and autumn. The *dv/v* of these two stations mainly decrease and increase when rainfall begins and stops, respectively (black and blue curves). At the station TDCB, rainfall distributes more uniformly throughout the year compared to the aforementioned two stations with the *dv/v* dropping to a minimum after the primary rainy season. In northern Taiwan, the rainfall pattern is different from other places of Taiwan, as indicated by the data at the station WFSB, whereas the decline of *dv/v* in November can be observed after the rainy season in wintertime.

3.2. Effect of Rainfall-Induced Pore Pressure Changes on Seismic Velocity Variations

The qualitative match seen between the *dv/v* and the rainy season suggests a possible influence of rainfall. Rainfall-induced pore pressure changes rather than rainfall itself have been suggested to cause the seismic velocity variations in many places (Andajani et al., 2020; Donaldson et al., 2019; Liu et al., 2020; Rivet et al., 2015; Wang et al., 2017). Therefore, we use a one-dimensional fully coupled diffusion equation (Talwani et al., 2007) to compute the pore pressure changes. The pore pressure change, $P(r, t)$, can be expressed as a function of diffusion distance (r) and time (t) from daily precipitation p_i at the surface and at day t:

$$P(r,t) = \sum_{i=1}^{n} \delta p_i erfc\left[\frac{r}{\left(4c(n-i)\delta t\right)^{1/2}}\right], \tag{2}$$

where n indicates the number of time increments δt from the day of the rainfall to the time t, δp_i is the precipitation load changes ($\rho \cdot g \cdot \delta h_i$) at the sampled instant t_i, c is the diffusion rate (m^2/s), and *erfc(x)* is the complementary error function. The distance r here is considered as an effective depth corresponding to the peak of sensitivity kernels as ~2 km (Figure S4). We can consider a linear relationship between $\delta v/v$ and pore pressure change P:

$$\frac{\delta v}{v}_{\text{pred}} = A \cdot P + B, \tag{3}$$

where A is an amplification factor represented as $cov\left(\frac{\delta v}{v}(t), P(t)\right)/var\left(P(t)\right)$ and B is a constant (Rivet et al., 2015; Wang et al., 2017). We then find the diffusion rate, c, using grid search method, in a range of 0.1–10 to fit the *dv/v* by minimizing the misfit of square residuals σ^2:

$$\sigma^2(c) = \frac{1}{n}\sum_{i=1}^{n}\left(\frac{\delta v}{v}(i) - \frac{\delta v}{v}_{\text{pred}}(i,c)\right)^2. \tag{4}$$

To avoid possible bias due to coseismic *dv/v* drops and subsequent recovery trends during the grid search (Figures 1d and 1e), the fitting only uses the data within a certain time period without clear earthquake-induced signals (Figure S7). The sought out diffusion rate is then used to calculate the pore pressure changes and the predicted *dv/v* for the entire time period. Figure S7 demonstrates how we estimate the predicted *dv/v* from rainfall at Station NACB. Using the Gaussian smoothed rainfall record as an input, we obtain a diffusion rate of ~1 m^2/s and a correlation coefficient value of ~0.8. We note that changing different

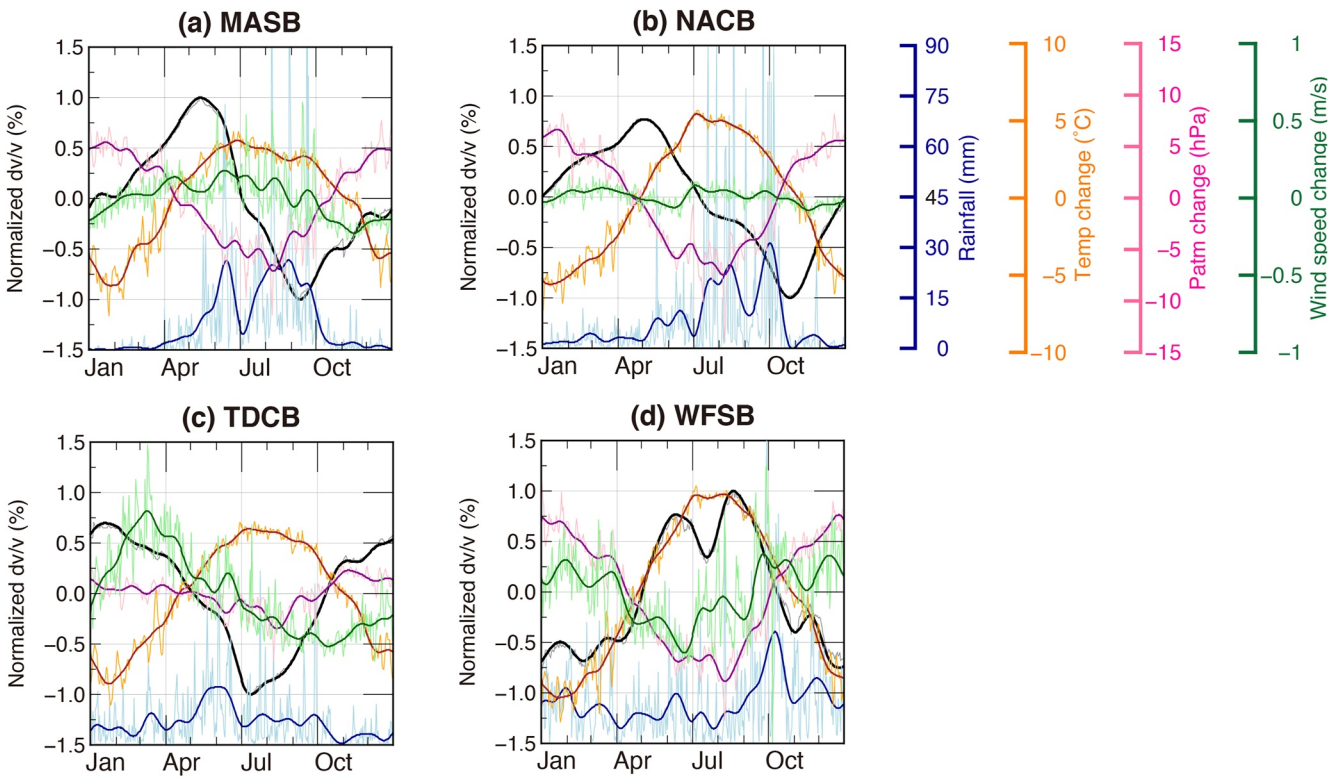

Figure 5. The year-average examples of the (a) Station MASB in southern Taiwan, (b) Station NACB in eastern Taiwan, (c) Station TDCB in central Taiwan, and (d) Station WFSB in northern Taiwan. Each subplot has the normalized-*dv/v* in black and the corresponding rainfall (blue), changes of temperature (orange), air pressure (purple), and wind speed (green) changes.

timeperiods gives similar results in general (Figure S7). According to the correlation coefficients, the predicted *dv/v* could overall explain 60%–80% of the *dv/v* variations for most stations (Figures S7 and S8). The cross-correlation coefficient (CC) and corresponding time shift (dT) between the long-term time series of *dv/v* and all other environmental data (with 30-day low-pass filtering) for each station are also calculated in Table S2. Similar to Figure 5, we show the comparison of annual stacks between the observed *dv/v* and the predicted *dv/v* derived from rainfall-induced pore pressure changes at the four representative stations in Figure 6.

3.3. Coseismic *dv/v* Drops Related to Regional Earthquakes

In addition to the strong periodic signals, clear coseismic drops followed by a long increasing trend in *dv/v* are also observed and most pronounced at Station SSLB (Figures 1b–1e). We confirm with the weather data near Station SSLB that this trend is not related to any long-term environmental changes (Figure S9) and mainly represents the post-seismic relaxation process of the 1999 Chi-Chi earthquake (the red star in Figure 1) as investigated by Tang et al. (2019) and observed for many earthquakes (Hobiger et al., 2012; Qiu et al., 2020; Wegler & Sens-Schönfelder, 2007). The largest *dv/v* drop of −0.6% (from 0.4% to −0.2%) related to the 1999 M_w 7.6 Chi-Chi earthquake is observed at Station SSLB which is closest to the rupture zone. This value is compatible with and among the high values of other coseismic *dv/v* observations of $M > 6$ earthquakes (Liu et al., 2018). Note that different preprocessing, coda window length for measuring, and spatial and temporal averaging may also affect the results. The coseismic *dv/v* drop and subsequent recovery are also observed at distant stations but greatly masked by periodic *dv/v* variations (e.g., Station NACB). We also find other plausible coseismic *dv/v* drops related to the 2003 M_w 6.8 Chengkung earthquake (purple star), the 2006 M_w 6.4 Taitung earthquake (green star), and the 2018 M_w 6.4 Hualien earthquake (blue star) but they are less pronounced than the 1999 M_w 7.6 Chi-Chi earthquake due to relatively small coseismic drops and large periodic variations in *dv/v*.

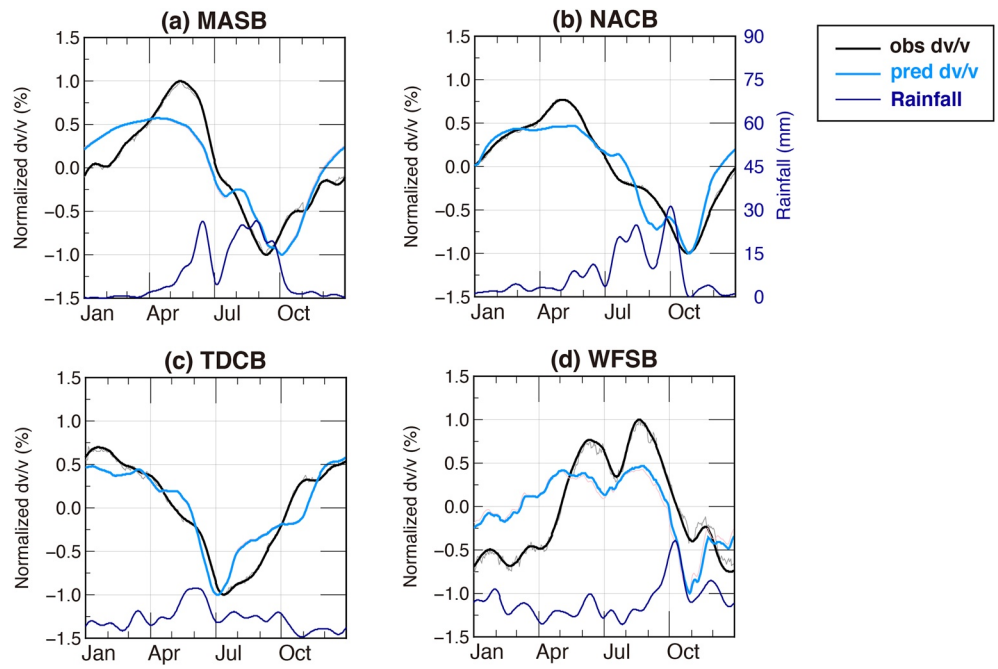

Figure 6. Annual stacks of the observed (black), predicted (blue) d*v/v*, and rainfall (dark blue) at four stations shown in Figure 4.

4. Discussion

4.1. Predominant Factor Driving the Seasonal Velocity Variations

We normalize and color code the annual stacks of *dv/v*, environmental data, and calculate pore pressure changes at all stations in Figure 7. It is clearer that the temporal variations of temperature and air pressure are similar across Taiwan (Figures 7c and 7f) and inconsistent with the site-dependent characteristics observed in *dv/v* (Figure 7a). The variations of wind speed (and therefore the induced local noise wavefields) are site-dependent (Figure 7b) but more complex than the *dv/v* variations with small-scale fluctuations. Alternatively, the site-dependent rainfall patterns (Figure 7e) not only fit with the *dv/v* decline periods qualitatively (Figures 5 and 7a); but through the pore pressure change modeling (Figure 7d), their modeled *dv/v* also captures the first-order features of the observed *dv/v* remarkably (Figure 7g). From correlations between the *dv/v* with different factors (Table S2), the rainfall-induced pore pressure change is also the one that could fit most of the stations simultaneously with overall high CC (mostly above 0.5) values, and therefore seems to play a predominant role of the seasonal *dv/v* variations in Taiwan.

Previous studies have found multiple factors influencing seismic velocity changes worldwide. Wang et al. (2017) observed a combination of effects from pore pressure, snow thickness, and sea-level changes on the seasonal variations of *dv/v* from region to region throughout Japan. Donaldson et al. (2019) analyzed a decade-long *dv/v* in the northern volcanic zones of Iceland and found that seasonal *dv/v* cycles reflect the elastic responses of the loads of snow, air pressure, and groundwater. Liu et al. (2020) investigated the temporal evolution of *dv/v* in the Mississippi embayment and found that seasonal *dv/v* correlate primarily with groundwater level variations. The residual *dv/v* variations further correlate with the air pressure in the short term and with temperature in the long term after removing the groundwater effect. We also investigate the residual *dv/v* variations by removing the *dv/v* from the rainfall effect but find no significant correlations with other factors on a regional scale (Figures 7i, S10b, and S10d). Temperature seems to take some effect but locally at the WARB station (correlation coefficients 0.57) in eastern Taiwan (Figure S10a).

Seasonal variations of noise sources are one of the common concerns causing spurious seasonal *dv/v* variations (Zhan et al., 2013). We note the noise sources here mainly refer to the ocean microseism (considering the 0.1–0.9 Hz frequency band) and should distinguish itself from wind-induced noise (Hillers et al., 2015).

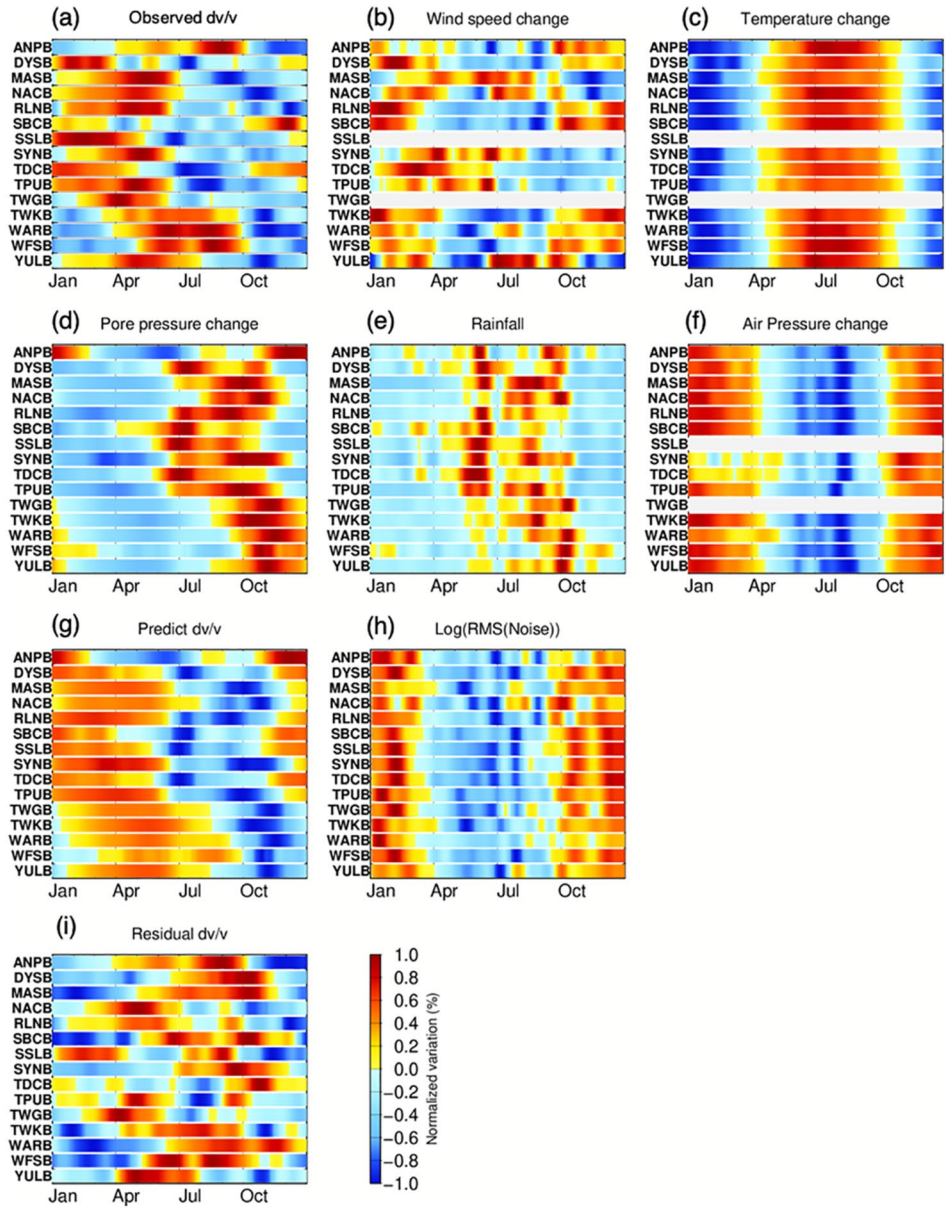

Figure 7. Normalized annual stacks at all stations. (a) Observed *dv/v*. (b) Wind speed change. (c) Temperature change. (d) Rainfall induced pore pressure change. (c) Rainfall change. (f) Air pressure change. (g) Predicted *dv/v* via the calculation in Section 3.2. (h) The root-mean-square of the noise amplitude. (i) The residual *dv/v* estimated by correcting the rainfall-induced *dv/v* from observations.

Liu et al. (2020) found that the decrease of noise amplitude can induce a small increase in *dv/v* in the Mississippi Embayment but the level of noise-induced *dv/v* variations is much less than that caused by pore pressure changes in the crust and sediments. To examine the possible bias from the noise variations, we also calculate the root mean square (RMS) of the noise amplitude of three components within the frequency band of 0.1–0.9 Hz (Figure S10). The annual stacks of the noise amplitude RMS generally show high-energy noise (warm color) during winter and low energy noise (cold color) during summer (Figure 7h). Since Taiwan is a relatively small island, it is reasonable to observe coherent spatial variations related to the dry and wet seasons across the entire island. While the noise amplitude does vary seasonally, the relatively uniform pattern across most stations is not in phase with either the observed *dv/v* or the residual *dv/v* variations in general (Figures 7a and 7i). A slightly negative correlation might be found locally for some stations, such

as at Station WARB where the correlation coefficient is −0.36 (Figure S10a). Its effect on *dv/v*, if exists, is likely secondary.

4.2. Groundwater Modeling and the Hydrological Model

The high correlation between the *dv/v* variations and rainfall-induced pore pressure changes implies a vertically efficient hydrological process that allows the rainfall to infiltrate into shallow crust. To verify this condition, we model the temporal evolution of groundwater level using the rainfall data at the 10 selected sites where the groundwater station and weather station are nearly collocated (the yellow circles and green squares in Figure S11). Except the station in the Puli basin, all the station pairs are within 1 km (Table S1). We model the groundwater level (GWL) using the equation proposed by Sens-Schönfelder and Wegler (2006)

$$\mathrm{GWL}\left(t_i\right) = \mathrm{GWL}_0 + \sum_{n=0}^{i} \frac{p\left(t_n\right)}{\varphi} e^{\left(-a\left(t_i - t_n\right)\right)}, \tag{5}$$

where φ is porosity, a is the parameter describing the decay, GWL_0 is the asymptotic water level, and $p(t_n)$ denotes the daily precipitation. The results show excellent fits of groundwater variations in the foothill and mountainous regions (correlation coefficients greater than 0.9) but poor fits in plain areas such as in the Taipei basin and Tainan plain (Figure S11). Due to the cover of thick sediments in plain and basin areas, the recharge of groundwater is likely from upstream and laterally at depths (Hsu, Fu, et al., 2020). In contrast, the good fits with time shifts within one day suggest an effective and rapid vertical/subvertical infiltration process in the mountainous and foothill areas. The active deformation in fold-and-thrust belts in the western foothills and extensive shallow normal-faulting activity in the mountain ranges may produce fractures and allow effective fluid infiltration (Hsu et al., 2009; Wu et al., 2008). Spatially, we also obtain worse fits between *dv/v* and rainfall-induced pore pressure changes (cross-correlations coefficient <0.6) for the stations in the plain and basin-edge areas (e.g., RLNB and ANPB) and better fits for the stations in the mountainous areas (cross-correlation coefficient >0.6) shown in Figure 8a. The fits for the basin/plain site stations are likely due to the undrained regime where groundwater levels can be maintained by human activities such as reservoirs, groundwater management, and agriculture/irrigation.

Among all the data, there is one seismic station (MASB) near groundwater and weather stations (Figure 9a), offering a good opportunity to confirm the relationships between *dv/v*, rainfall, and groundwater variations. Figure 9b shows significant similarities between the time series of *dv/v* with the observed groundwater level, and *dv/v* with the modeled pore-pressure changes from rainfall. The negative correlation between the *dv/v* and the groundwater level indicates that a rise of groundwater increases the pore pressure in the saturated medium below and then decreases the seismic velocities (Clements & Denolle, 2018; Grêt et al., 2006; Vidal et al., 2021). While groundwater recharge from rainfall depends on infiltration capacity, soil type, vegetation, and topography, the satisfactory fit through our groundwater modeling (Equation 5) suggests a relatively intimately linked hydrologic system in the shallow crust of the foothill and mountain areas in Taiwan. Since there are generally no groundwater stations in the mountainous areas (Figure S5b), the rainfall could be used as a good proxy to calculate the pore pressure changes and correlate with *dv/v* variations (Figures 7 and 9).

Our study suggests that the observed seasonal *dv/v* variations (Figure 1) are dominantly due to pore pressure diffusion. As shown in Figure 10, when there is no rainfall (Period A), the seismic velocity changes are due to the state changes of pore pressure caused by groundwater level variations. When rainfall season begins (Period B), sufficient amounts of water infiltrates and percolates downward into the groundwater system through the fractured uppermost crust (Figure S11). In Period C, once the groundwater rises, the diffusion front starts to propagate downward and pore pressure change reach its peak when the seismic velocity drops to its minimum (Figures 6 and 7). When the groundwater level gradually returns to the background (Period A), the pore pressure reduces and the seismic velocity then recovers. We further examine this idea utilizing the lapse-time-dependence test (Obermann et al., 2016; Qiu et al., 2020) with four 20-sec-long coda windows from 10 to 60 s lag time. As shown in Figure S12, the results show that the *dv/v* variations have similar amplitudes for most stations, although the later windows temporally show slightly

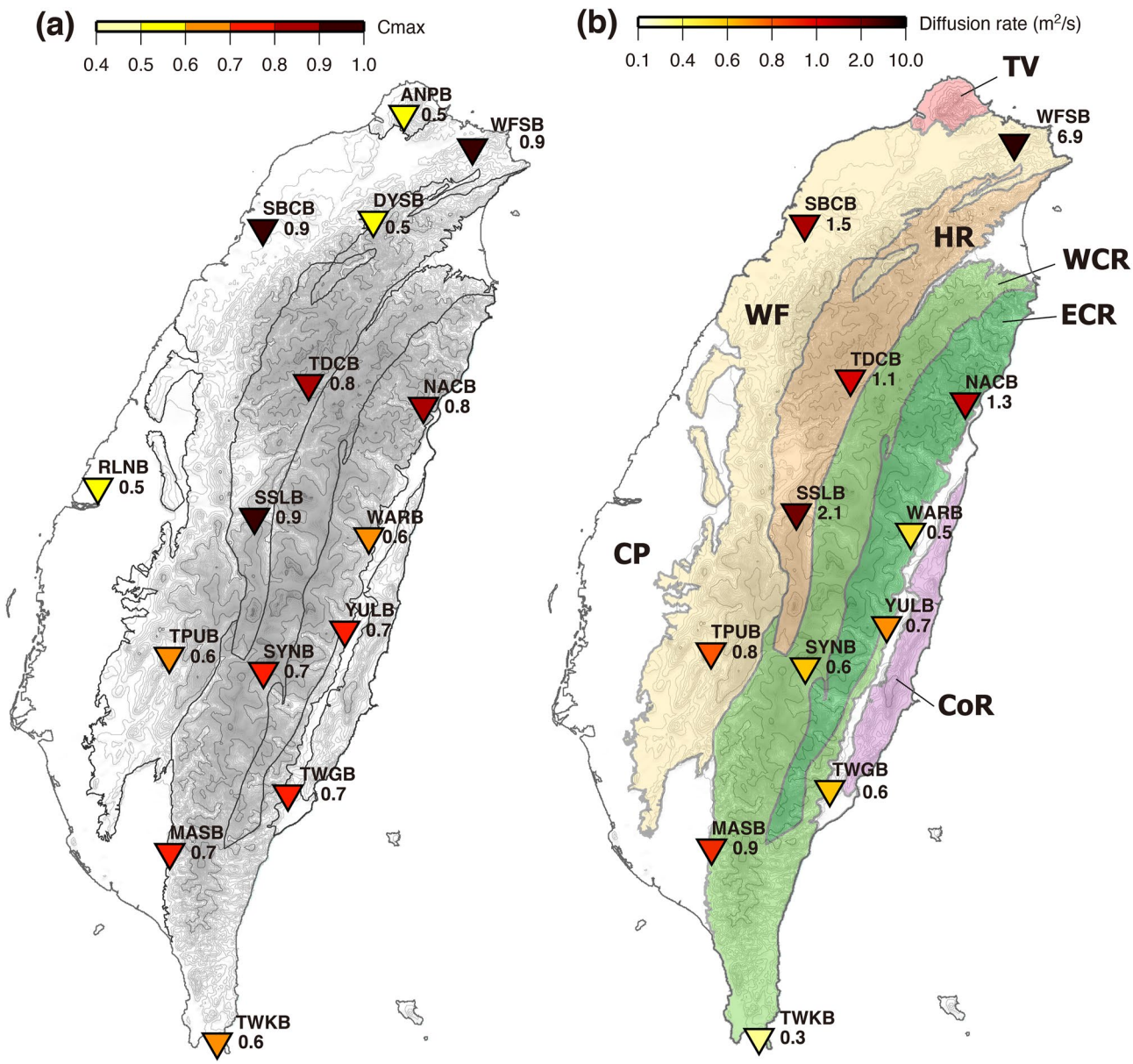

Figure 8. Spatial distribution of (a) the correlation coefficients (C_{max}) between the observed and predicted *dv/v* and (b) corresponding diffusion rate at which $C_{max} > 0.6$. The geological units in (b) from west to east are the Coastal Plain (CP): alluvial sediments; Western Foothills (WF): thick sequence of shallow marine to shelf clastic sediments; Hsueshan Range (HR): slate belt with widespread meta-sandstone; Western Central Range (WCR): slate belt with higher grade of metamorphism; Eastern Central Range (ECR): Metamorphic complex composed of schist, marble, and gneiss; Coastal Range (CoR): northern extension of the Luzon volcanic arc; and Tatun Volcano group (TV): postcollision extensional volcanism (Ho, 1986).

weaker or slightly stronger amplitudes (Figures S12a–S12c). This indicates that the medium changes are at least not very near surface (e.g., groundwater variations) as we proposed. In contrast, the RLNB station shows much stronger variations at early coda. This corroborates that stations at the plain/basin areas with thicker sediments are subject to more complex hydrological processes (Figure S12d). Other environmental factors such as temperature, air pressure, and wind speed can have an effect but they seem to secondary or below the *dv/v* uncertainty to measure in Taiwan at an annual scale.

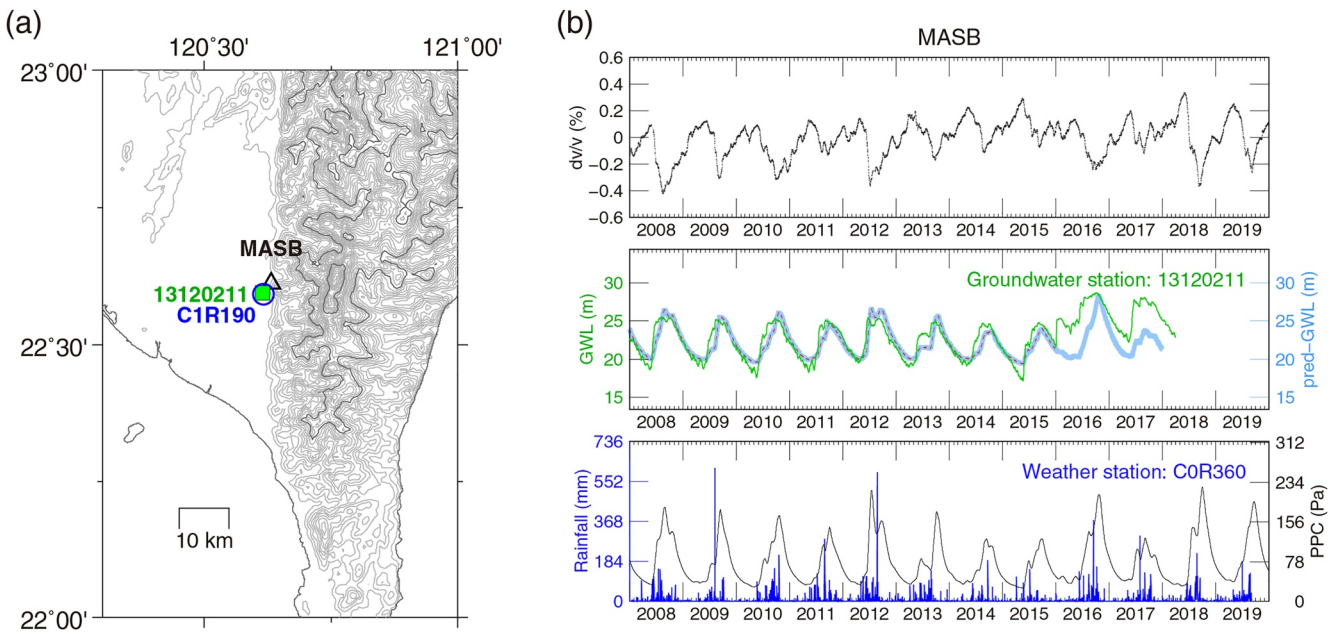

Figure 9. An example of groundwater modeling for Station MASB. (a) Station locations of seismic (black triangle), weather (blue circle), and groundwater stations (green square). (b) Time evolution of *dv/v* (top), observed and modeled groundwater levels (middle), rainfall, and rainfall-induced pore pressure changes (bottom). The red dashed curve shows the time period used for groundwater modeling.

4.3. Spatial Distribution of Diffusivity

Fitting the observed *dv/v* with rainfall-induced pore pressure change provides the diffusivity estimates (Figure S7). As discussed in the previous section, the presence of thick sediments and lateral hydrological processes in the basin/plain areas degrade the fitting for ANPB and RLNB stations. Therefore, we only plot the diffusion rate for the stations with high correlation coefficients above 0.6 (Figure 8b). The estimates of diffusivity fall reasonably in the range of 0.1–10 m^2/s as reported in previous studies (Hsu, Huang, et al., 2020; Talwani et al., 2007). Using a similar approach in the same 0.1–0.9 Hz frequency band, Andajani et al. (2020) estimated diffusion rates ranging from 0.02 to 1.0 m^2/s for the Chugoku and Shikoku regions in southwestern Japan. They found that the correlations between the pore pressure changes and *dv/v* differ between locations, with clear correlations observed at the stations in granitic regions but not in the steep mountain areas. In this study, most of the stations sit in the areas of sedimentary and low-grade metamorphic rocks (e.g., sandy shale, siltstone, slate, and meta-sandstone) except for Station NACB and YULB which are located at areas with high-grade metamorphic rocks (marble, and black schist). No apparent relationship between the lithology and diffusivity is observed from our analysis. This, however, does not preclude a possible relationship with lithology when analyzing the *dv/v* at higher frequency bands (e.g., 1–20 Hz) as found in Viens et al. (2018) in the greater Tokyo area of Japan.

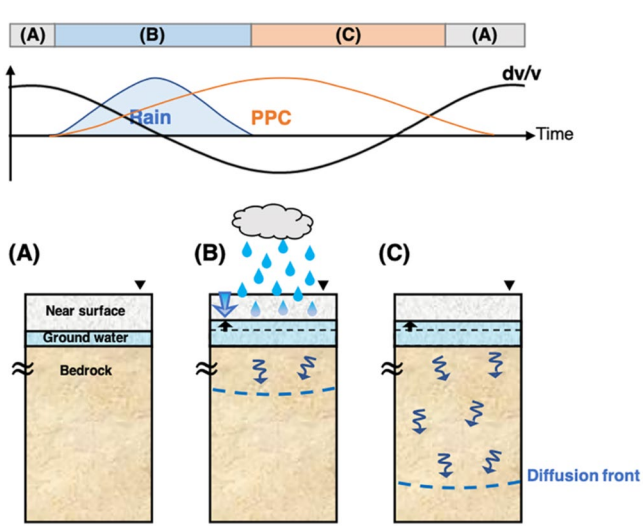

Figure 10. Hypothetical model of the crustal seismic velocity responses in Taiwan. The time series of *dv/v* and rainfall-induced pore pressure change (PPC) shown on the top subplot with three periods A–C (top). The open blue arrow indicates rainfall infiltration into the bedrock. The thick black arrow indicates changes in groundwater level. The blue curvy arrows represent the pore pressure diffusion driven by the rapid rise of groundwater level after rainfall.

The lack of correlation between the pore pressure changes and *dv/v* in the deep mountain areas in Andajani et al. (2020) also seems contradictory to our observations, where the good correlations appear mainly at the stations in the foothill and mountain areas. We believe both observations can be explained from fracture development controlled by different lithology and tectonic activity. The active deformation in the fold-and-thrust belts and extension revealed by quartz veins (Chan et al., 2005) and normal-faulting events (Hsu et al., 2009) in the Central Range likely

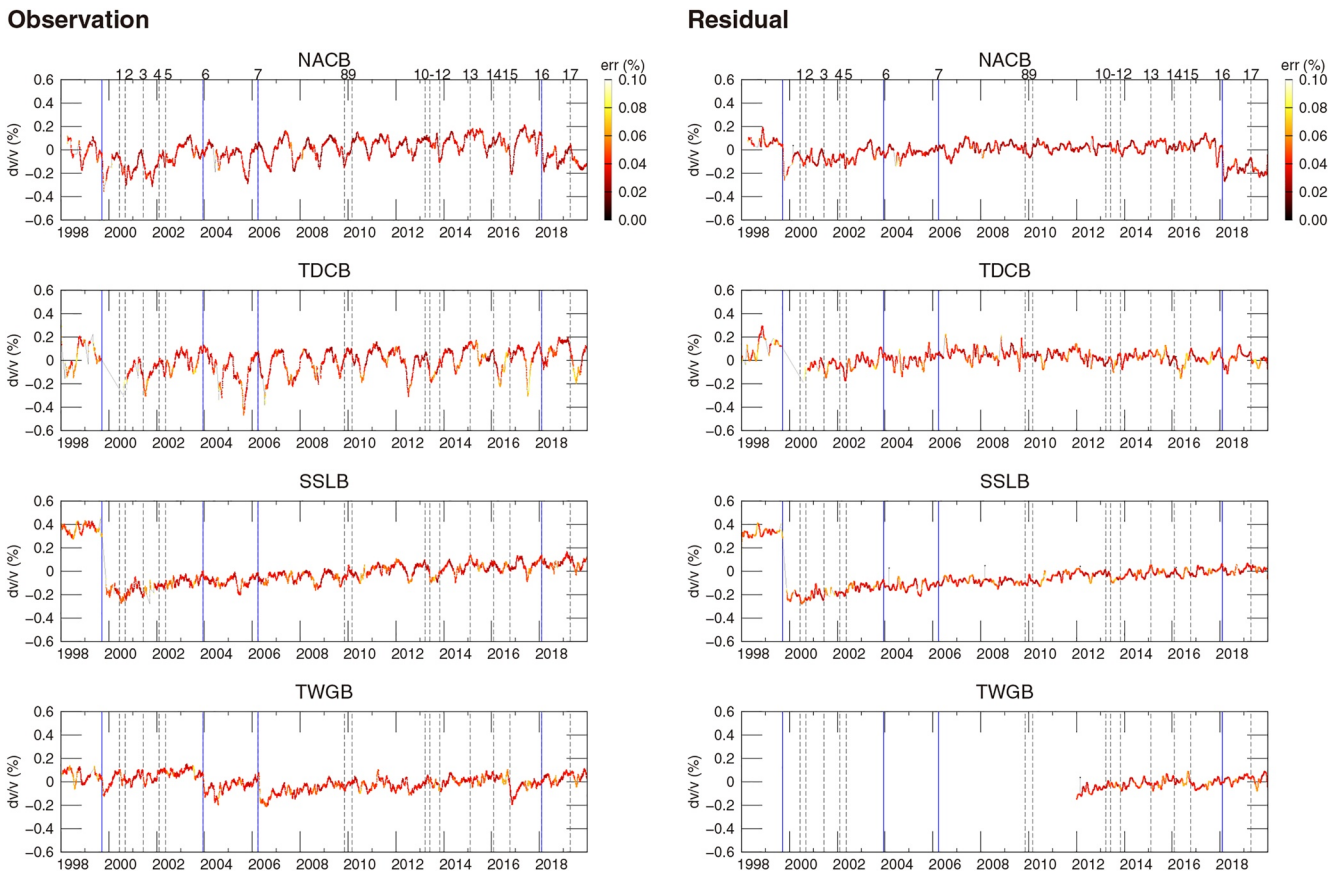

Figure 11. The time series of *dv/v* before (left) and after (right) correcting the rainfall-induced *dv/v* changes. Station locations are referred to Figure 1. The blue lines mark the occurrence time of earthquakes in Figure 1a with clear (solid) and unclear (dashed) coseismic offsets. The black dashed lines mark the occurrence time for all earthquakes with $M > 6$ and depths <30 km in Taiwan. Earthquake locations are shown in Figure S14.

produced fractures that allow effective fluid infiltration in the shallow crust. A relatively smaller hydraulic diffusivity c (<1 m^2/s) is found in eastern Taiwan and suggests a longer delay between the rainfall and pore pressure changes. This distinct hydraulic property may be a consequence of different tectonic settings between the east and the west. The analysis demonstrates a potential for seismology to infer hydraulic properties of the shallow crust without well data (Clements & Denolle, 2018; Vidal et al., 2021).

4.4. Improving Detection Capability of Coseismic *dv/v* Drops

By ambient noise interferometry, understanding and correcting the external effect from the *dv/v* variations is an important step toward monitoring internal crustal processes (Donaldson et al., 2019; Rivet et al., 2015; Wang et al., 2017). There are two frequently used methods to correct the seasonal periodicity in *dv/v* variations. One is based on the empirical transfer functions from actual weather data as was done by Rivet et al. (2015) and Wang et al. (2017). The other is a curve-fitting approach as in Hobiger et al. (2012) and Qiu et al. (2020). While seasonal/periodic signals may be corrected by curve-fitting approaches that consider multiple basis functions, we demonstrate a few cases here to address the advantage and necessity of using rainfall data for more realistic correction. Figure 11 shows the *dv/v* variations before and after the correction for selected stations, marked with the occurrence times of moderate-to-large earthquakes. Taking Station NACB as an example, the shape of the *dv/v* drop associated with the 1999 M_w 7.6 Chi-Chi earthquake is actually indistinguishable from the rainfall-induced annual *dv/v* drops. However, after correcting the rainfall-induced pore pressure effect, the coseismic velocity drops clearly stand out for the 1999 M_w 7.6 Chi-Chi earthquake and also for the 2018 M_w 6.4 Hualien earthquake. Another good example is Station TWGB, which shows less pronounced seasonal *dv/v* variations but four clear coseismic-like *dv/v* drops.

The timing of the first three co-seismic *dv/v* drops correspond to the 1999 M_w 7.6 Chi-Chi earthquake, 2003 M_w 6.8 Chengkung earthquake, and 2006 M_w 6.4 Taitung earthquake, respectively. But for the fourth drop, while the timing seems to be close to one offshore moderate earthquake (Event 15 in Figure S13), it can be removed after correcting for the rainfall related signal during Typhoon Meranti in 2016. The correction is only implemented after 2012 because the nearby weather station was installed then. For the station such as SSLB that shows a clear co-seismic *dv/v* drop before correction, correcting external effects is still beneficial for better assessing seismic velocity recovery and healing rate that could provide valuable insight into post-seismic stress relaxation (Brenguier, Campillo, et al., 2008) and crustal rheology (Tang et al., 2019).

5. Conclusions

We apply the ambient noise single-station cross-component technique to analyze continuous seismic data in 1998–2019. The results reveal coseismic drops as well as strong seasonal variations in seismic velocity changes (*dv/v*) in Taiwan. By systematically comparing the annual variations of *dv/v*, rainfall, air pressure, temperature, wind speed, and groundwater, in both time and frequency domains, we discuss possible physical mechanisms for the observed seasonality in *dv/v*. Our results suggest that annual rainfall and its induced pore pressure change is the principal driver for seasonal *dv/v* variations in Taiwan. Using a 1-D hydrological diffusion equation and a linear relationship between the pore pressure changes and *dv/v*, we find good agreement between the observed and predicted *dv/v* variations with correlation coefficients of 0.6–0.9 at stations located in mountainous and foothill regions. While the groundwater modeling also shows a high correlation (CC > 0.9) between rainfall and groundwater level variations with a short time delay (<1 day), the examination of the coda lapse-time dependence suggest that the medium changes are not near the surface (e.g., groundwater variations). This corroborates that the *dv/v* seasonality is mainly caused by the pore pressure changes at depths as a hydrological diffusion model we proposed in Figure 10. Further frequency-dependent studies of *dv/v* may help resolve changes of hydrological parameters at depths in more details.

More importantly, evaluating (external) environmental influences on *dv/v* allows us to possibly isolate (internal) crustal damage related to earthquakes. By correcting the effect of rainfall-induced pore pressure changes, we demonstrate an improvement for detecting coseismic *dv/v* drops for regional moderate-to-large earthquakes. This study paves the way for monitoring and investigating the crustal tectonic processes of Taiwan, such as fault zone damage and healing, with more accuracy in the future.

Data Availability Statement

All processed cross-correlation functions are made to open access in a Harvard Dataverse reciprocity (https://doi.org/10.7910/DVN/GU2OTC).

Acknowledgments
The authors thank Alex Song and Fan-Chi Lin for valuable discussion and Kyle Smith for helping improve the manuscript. They thank for the waveform data provided by the Broadband Array in Taiwan for Seismology (http://bats.earth.sinica.edu.tw/). They thank the editor Yehuda Ben-Zion, associated editor Nikolai Shapiro, and two reviewers, Gregor Hillers and Marine Denolle, for their constructive comments that significantly helped improve the manuscript. This work was supported by the Ministry of Science and Technology of Taiwan (Grant 109-2116-M-001-011).

References

Andajani, R. D., Tsuji, T., Snieder, R., & Ikeda, T. (2020). Spatial and temporal influence of rainfall on crustal pore pressure based on seismic velocity monitoring. *Earth Planets and Space*, *72*(1), 1–17. https://doi.org/10.1186/s40623-020-01311-1

Bennington, N., Haney, M., Thurber, C., & Zeng, X. (2018). Inferring magma dynamics at Veniaminof Volcano via application of ambient noise. *Geophysical Research Letters*, *45*(21), 11–650. https://doi.org/10.1029/2018GL079909

Bensen, G. D., Ritzwoller, M. H., Barmin, M. P., Levshin, A. L., Lin, F., Moschetti, M. P., et al. (2007). Processing seismic ambient noise data to obtain reliable broad-band surface wave dispersion measurements. *Geophysical Journal International*, *169*(3), 1239–1260. https://doi.org/10.1111/j.1365-246X.2007.03374.x

Berbellini, A., Zaccarelli, L., Faenza, L., Garcia, A., Improta, L., De Gori, P., & Morelli, A. (2021). Effect of groundwater on noise-based monitoring of crustal velocity changes near a produced water injection well in Val d'Agri (Italy). *Frontiers of Earth Science*, *9*, 197. https://doi.org/10.3389/feart.2021.626720

Brenguier, F., Campillo, M., Hadziioannou, C., Shapiro, N. M., Nadeau, R. M., & Larose, E. (2008). Postseismic relaxation along the San Andreas Fault at Parkfield from continuous seismological observations. *Science*, *321*(5895), 1478–1481. https://doi.org/10.1126/science.1160943

Brenguier, F., Shapiro, N. M., Campillo, M., Ferrazzini, V., Duputel, Z., Coutant, O., & Nercessian, A. (2008). Towards forecasting volcanic eruptions using seismic noise. *Nature Geoscience*, *1*(2), 126–130. https://doi.org/10.1038/ngeo104

Chan, Y.-C., Okamoto, K., Yui, T.-F., Iizuka, Y., & Chu, H.-T. (2005). Fossil fluid reservoir beneath a duplex fault structure within the Central Range of Taiwan: Implication for fluid leakage and lubrication during earthquake rupturing process. *Terra Nova*, *17*, 493–499. https://doi.org/10.1111/j.1365-3121.2005.00636.x

Clarke, D., Zaccarelli, L., Shapiro, N. M., & Brenguier, F. (2011). Assessment of resolution and accuracy of the Moving Window Cross Spectral technique for monitoring crustal temporal variations using ambient seismic noise. *Geophysical Journal International*, *186*(2), 867–882. https://doi.org/10.1111/j.1365-246X.2011.05074.x

Clements, T., & Denolle, M. A. (2018). Tracking groundwater levels using the ambient seismic field. *Geophysical Research Letters*, *45*(13), 6459–6465. https://doi.org/10.1029/2018GL077706

De Plaen, R. S., Lecocq, T., Caudron, C., Ferrazzini, V., & Francis, O. (2016). Single-station monitoring of volcanoes using seismic ambient noise. *Geophysical Research Letters*, *43*(16), 8511–8518. https://doi.org/10.1002/2016GL070078

Donaldson, C., Winder, T., Caudron, C., & White, R. S. (2019). Crustal seismic velocity responds to a magmatic intrusion and seasonal loading in Iceland's Northern Volcanic Zone. *Science Advances*, *5*(11), eaax6642. https://doi.org/10.1126/sciadv.aax6642

Feng, K. F., Huang, H. H., & Wu, Y. M. (2020). Detecting pre-eruptive magmatic processes of the 2018 eruption at Kilauea, Hawaii volcano with ambient noise interferometry. *Earth Planets and Space*, *72*, 1–15. https://doi.org/10.1186/s40623-020-01199-x

Grêt, A., Snieder, R., & Özbay, U. (2006). Monitoring in situ stress changes in a mining environment with coda wave interferometry. *Geophysical Journal International*, *167*(2), 504–508. https://doi.org/10.1111/j.1365-246X.2006.03097.x

Herrmann, R. B. (1987). Surface wave inversion. *Computer programs in seismology* (p. 4). Saint Louis University.

Hillers, G., & Ben-Zion, Y. (2011). Seasonal variations of observed noise amplitudes at 2–18 Hz in southern California. *Geophysical Journal International*, *184*(2), 860–868. https://doi.org/10.1111/j.1365-246X.2010.04886.x

Hillers, G., Ben-Zion, Y., Campillo, M., & Zigone, D. (2015). Seasonal variations of seismic velocities in the San Jacinto fault area observed with ambient seismic noise. *Geophysical Journal International*, *202*(2), 920–932. https://doi.org/10.1093/gji/ggv151

Hillers, G., Campillo, M., Brenguier, F., Moreau, L., Agnew, D. C., & Ben-Zion, Y. (2019). Seismic velocity change patterns along the San Jacinto fault zone following the 2010 M 7.2 El Mayor-Cucapah and M 5.4 Collins Valley earthquakes. *Journal of Geophysical Research: Solid Earth*, *124*(7), 7171–7192. https://doi.org/10.1029/2018JB017143

Hillers, G., Campillo, M., & Ma, K. F. (2014). Seismic velocity variations at TCDP are controlled by MJO driven precipitation pattern and high fluid discharge properties. *Earth and Planetary Science Letters*, *391*, 121–127. https://doi.org/10.1016/j.epsl.2014.01.040

Ho, C. S. (1986). A synthesis of the geologic evolution of Taiwan. *Tectonophysics*, *125*, 1–16. https://doi.org/10.1016/0040-1951(86)90004-1

Hobiger, M., Wegler, U., Shiomi, K., & Nakahara, H. (2012). Coseismic and postseismic elastic wave velocity variations caused by the 2008 Iwate-Miyagi Nairiku earthquake, Japan. *Journal of Geophysical Research*, *117*(B9). https://doi.org/10.1029/2012JB009402

Hobiger, M., Wegler, U., Shiomi, K., & Nakahara, H. (2014). Single-station cross-correlation analysis of ambient seismic noise: Application to stations in the surroundings of the 2008 Iwate-Miyagi Nairiku earthquake. *Geophysical Journal International*, *198*(1), 90–109. https://doi.org/10.1093/gji/ggu115

Hsu, Y. F., Huang, H. H., Huang, M. H., Tsai, V. C., Chuang, R. Y., Feng, K. F., & Lin, S. H. (2020). Evidence for fluid migration during the 2016 Meinong, Taiwan, aftershock sequence. *Journal of Geophysical Research: Solid Earth*, *125*(9), e2020JB019994. https://doi.org/10.1029/2020JB019994

Hsu, Y. J., Fu, Y., Bürgmann, R., Hsu, S. Y., Lin, C. C., Tang, C. H., & Wu, Y. M. (2020). Assessing seasonal and interannual water storage variations in Taiwan using geodetic and hydrological data. *Earth and Planetary Science Letters*, *550*, 116532. https://doi.org/10.1016/j.epsl.2020.116532

Hsu, Y. J., Kao, H., Bürgmann, R., Lee, Y. T., Huang, H. H., Hsu, Y. F., et al. (2021). Synchronized and asynchronous modulation of seismicity by hydrological loading: A case study in Taiwan. *Science Advances*, *7*(16), eabf7282. https://doi.org/10.1126/sciadv.abf7282

Hsu, Y. J., Yu, S. B., Simons, M., Kuo, L. C., & Chen, H. Y. (2009). Interseismic crustal deformation in the Taiwan plate boundary zone revealed by GPS observations, seismicity, and earthquake focal mechanisms. *Tectonophysics*, *479*(1–2), 4–18. https://doi.org/10.1016/j.tecto.2008.11.016

Huang, H. H., Wu, Y. M., Song, X., Chang, C. H., Lee, S. J., Chang, T. M., & Hsieh, H. H. (2014). Joint Vp and Vs tomography of Taiwan: Implications for subduction-collision orogeny. *Earth and Planetary Science Letters*, *392*, 177–191. https://doi.org/10.1016/j.epsl.2014.02.026

Institute of Earth Sciences, Academia Sinica. (1996). *Broadband Array in Taiwan for seismology*. Institute of Earth Sciences, Academia Sinica. https://doi.org/10.7914/SN/TW

Le Breton, M., Bontemps, N., Guillemot, A., Baillet, L., & Larose, É. (2021). Landslide monitoring using seismic ambient noise correlation: Challenges and applications. *Earth-Science Reviews*, *216*, 103518. https://doi.org/10.1016/j.earscirev.2021.103518

Lecocq, T., Longuevergne, L., Pedersen, H. A., Brenguier, F., & Stammler, K. (2017). Monitoring ground water storage at mesoscale using seismic noise: 30 years of continuous observation and thermo-elastic and hydrological modeling. *Scientific Reports*, *7*(1), 1–16. https://doi.org/10.1038/s41598-017-14468-9

Liu, C., Aslam, K., & Daub, E. (2020). Seismic velocity changes caused by water table fluctuation in the New Madrid seismic zone and Mississippi embayment. *Journal of Geophysical Research: Solid Earth*, *125*(8), e2020JB019524. https://doi.org/10.1029/2020JB019524

Liu, Z., Huang, J., He, P., & Qi, J. (2018). Ambient noise monitoring of seismic velocity around the Longmenshan fault zone from 10 years of continuous observation. *Journal of Geophysical Research: Solid Earth*, *123*(10), 8979–8994. https://doi.org/10.1029/2018JB015986

Mao, S., Campillo, M., van der Hilst, R. D., Brenguier, F., Stehly, L., & Hillers, G. (2019). High temporal resolution monitoring of small variations in crustal strain by dense seismic arrays. *Geophysical Research Letters*, *46*(1), 128–137. https://doi.org/10.1029/2018GL079944

Mordret, A., Mikesell, T. D., Harig, C., Lipovsky, B. P., & Prieto, G. A. (2016). Monitoring southwest Greenland's ice sheet melt with ambient seismic noise. *Science Advances*, *2*(5), e1501538. https://doi.org/10.1126/sciadv.1501538

Obermann, A., Froment, B., Campillo, M., Larose, E., Planès, T., Valette, B., et al. (2014). Seismic noise correlations to image structural and mechanical changes associated with the Mw 7.9 2008 Wenchuan earthquake. *Journal of Geophysical Research: Solid Earth*, *119*(4), 3155–3168. https://doi.org/10.1002/2013JB010932

Obermann, A., Planes, T., Hadziioannou, C., & Campillo, M. (2016). Lapse-time-dependent coda-wave depth sensitivity to local velocity perturbations in 3-D heterogeneous elastic media. *Geophysical Journal International*, *207*(1), 59–66. https://doi.org/10.1093/gji/ggw264

Obermann, A., Planès, T., Larose, E., & Campillo, M. (2013). Imaging preeruptive and coeruptive structural and mechanical changes of a volcano with ambient seismic noise. *Journal of Geophysical Research*, *118*(12), 6285–6294. https://doi.org/10.1002/2013JB010399

Obermann, A., Planes, T., Larose, E., Sens-Schönfelder, C., & Campillo, M. (2013). Depth sensitivity of seismic coda waves to velocity perturbations in an elastic heterogeneous medium. *Geophysical Journal International*, *194*(1), 372–382. https://doi.org/10.1093/gji/ggt043

Olivier, G., Brenguier, F., Carey, R., Okubo, P., & Donaldson, C. (2019). Decrease in seismic velocity observed prior to the 2018 eruption of Kīlauea volcano with ambient seismic noise interferometry. *Geophysical Research Letters*, *46*(7), 3734–3744. https://doi.org/10.1029/2018GL081609

Pacheco, C., & Snieder, R. (2005). Time-lapse travel time change of multiply scattered acoustic waves. *Journal of the Acoustical Society of America*, *118*(3), 1300–1310. https://doi.org/10.1121/1.2000827

Planès, T., Larose, E., Margerin, L., Rossetto, V., & Sens-Schoenfelder, C. (2014). Decorrelation and phase-shift of coda waves induced by local changes: Multiple scattering approach and numerical validation. *Waves in Random and Complex Media*, *24*(2), 99–125. https://doi.org/10.1080/17455030.2014.880821

Qiu, H., Hillers, G., & Ben-Zion, Y. (2020). Temporal changes of seismic velocities in the San Jacinto Fault zone associated with the 2016 M w 5.2 Borrego Springs earthquake. *Geophysical Journal International*, *220*(3), 1536–1554. https://doi.org/10.1093/gji/ggz538

Richter, T., Sens-Schönfelder, C., Kind, R., & Asch, G. (2014). Comprehensive observation and modeling of earthquake and temperature-related seismic velocity changes in northern Chile with passive image interferometry. *Journal of Geophysical Research: Solid Earth*, *119*(6), 4747–4765. https://doi.org/10.1002/2013JB010695

Rivet, D., Brenguier, F., & Cappa, F. (2015). Improved detection of preeruptive seismic velocity drops at the Piton de La Fournaise volcano. *Geophysical Research Letters*, *42*(15), 6332–6339. https://doi.org/10.1002/2015GL064835

Seats, K. J., Lawrence, J. F., & Prieto, G. A. (2012). Improved ambient noise correlation functions using Welch′ s method. *Geophysical Journal International*, *188*(2), 513–523. https://doi.org/10.1111/j.1365-246X.2011.05263.x

Sens-Schönfelder, C., & Wegler, U. (2006). Passive image interferometry and seasonal variations of seismic velocities at Merapi Volcano, Indonesia. *Geophysical Research Letters*, *33*(21). https://doi.org/10.1029/2006GL027797

Snieder, R., Grêt, A., Douma, H., & Scales, J. (2002). Coda wave interferometry for estimating nonlinear behavior in seismic velocity. *Science*, *295*(5563), 2253–2255. https://doi.org/10.1126/science.1070015

Steer, P., Jeandet, L., Cubas, N., Marc, O., Meunier, P., Simoes, M., et al. (2020). Earthquake statistics changed by typhoon-driven erosion. *Scientific Reports*, *10*(1), 1–11. https://doi.org/10.1038/s41598-020-67865-y

Talwani, P., Chen, L., & Gahalaut, K. (2007). Seismogenic permeability, ks. *Journal of Geophysical Research*, *112*(B7). https://doi.org/10.1029/2006JB004665

Tang, C. H., Hsu, Y. J., Barbot, S., Moore, J. D., & Chang, W. L. (2019). Lower-crustal rheology and thermal gradient in the Taiwan orogenic belt illuminated by the 1999 Chi-Chi earthquake. *Science Advances*, *5*(2), eaav3287. https://doi.org/10.1126/sciadv.aav3287

Vidal, C. A., Zaccarelli, L., Pintori, F., Bragato, P. L., & Serpelloni, E. (2021). Hydrological effects on seismic-noise monitoring in karstic media. *Geophysical Research Letters*, *48*, e2021GL093191. https://doi.org/10.1029/2021GL093191

Viens, L., Denolle, M. A., Hirata, N., & Nakagawa, S. (2018). Complex near-surface rheology inferred from the response of greater Tokyo to strong ground motions. *Journal of Geophysical Research: Solid Earth*, *123*(7), 5710–5729. https://doi.org/10.1029/2018JB015697

Wang, Q. Y., Brenguier, F., Campillo, M., Lecointre, A., Takeda, T., & Aoki, Y. (2017). Seasonal crustal seismic velocity changes throughout Japan. *Journal of Geophysical Research: Solid Earth*, *122*(10), 7987–8002. https://doi.org/10.1002/2017JB014307

Wang, Q. Y., Campillo, M., Brenguier, F., Lecointre, A., Takeda, T., & Hashima, A. (2019). Evidence of changes of seismic properties in the entire crust beneath Japan after the Mw 9.0, 2011 Tohoku-oki Earthquake. *Journal of Geophysical Research: Solid Earth*, *124*(8), 8924–8941. https://doi.org/10.1029/2019JB017803

Weaver, R. L., Hadziioannou, C., Larose, E., & Campillo, M. (2011). On the precision of noise correlation interferometry. *Geophysical Journal International*, *185*(3), 1384–1392. https://doi.org/10.1111/j.1365-246X.2011.05015.x

Wegler, U., & Sens-Schönfelder, C. (2007). Fault zone monitoring with passive image interferometry. *Geophysical Journal International*, *168*(3), 1029–1033. https://doi.org/10.1111/j.1365-246X.2006.03284.x

Wu, Y. M., Zhao, L., Chang, C. H., & Hsu, Y. J. (2008). Focal-mechanism determination in Taiwan by genetic algorithm. *Bulletin of the Seismological Society of America*, *98*(2), 651–661. https://doi.org/10.1785/0120070115

Yu, T. C., & Hung, S. H. (2012). Temporal changes of seismic velocity associated with the 2006 Mw 6.1 Taitung earthquake in an arc-continent collision suture zone. *Geophysical Research Letters*, *39*(12). https://doi.org/10.1029/2012GL051970

Yuan, C., Bryan, J., & Denolle, M. (2021). Numerical comparison of time-, frequency-and wavelet-domain methods for coda wave interferometry. *Geophysical Journal International*, *226*(2), 828–846. https://doi.org/10.1093/gji/ggab140

Zhan, Z., Tsai, V. C., & Clayton, R. W. (2013). Spurious velocity changes caused by temporal variations in ambient noise frequency content. *Geophysical Journal International*, *194*(3), 1574–1581. https://doi.org/10.1093/gji/ggt170